

Augmented reality simulation framework for minimally invasive orthopedic surgery

*Original*

Augmented reality simulation framework for minimally invasive orthopedic surgery / Cangelosi, Antonio; Riberi, Giacomo; Titolo, Paolo; Salvi, Massimo; Molinari, Filippo; Ulrich, Luca; Vezzetti, Enrico; Agus, Marco; Cali, Corrado. - In: COMPUTERS IN BIOLOGY AND MEDICINE. - ISSN 0010-4825. - 189:(2025), pp. 1-16.  
[10.1016/j.combiomed.2025.109943]

*Availability:*

This version is available at: 11583/2998307 since: 2025-03-19T09:36:44Z

*Publisher:*

Elsevier

*Published*

DOI:10.1016/j.combiomed.2025.109943

*Terms of use:*

This article is made available under terms and conditions as specified in the corresponding bibliographic description in the repository

*Publisher copyright*

Elsevier postprint/Author's Accepted Manuscript

© 2025. This manuscript version is made available under the CC-BY-NC-ND 4.0 license  
<http://creativecommons.org/licenses/by-nc-nd/4.0/>. The final authenticated version is available online at:  
<http://dx.doi.org/10.1016/j.combiomed.2025.109943>

(Article begins on next page)

# Augmented Reality Simulation Framework for Minimally Invasive Orthopedic Surgery

Antonio Cangelosi<sup>1,2,3†</sup>, Giacomo Riberi<sup>1,3,4†</sup>, Paolo Titolo<sup>5</sup>,  
Massimo Salvi<sup>2</sup>, Filippo Molinari<sup>2</sup>, Luca Ulrich<sup>6</sup>,  
Enrico Vezzetti<sup>6</sup>, Marco Agus<sup>7</sup>, Corrado Cali<sup>1,3,8\*</sup>

<sup>1</sup>Intravides SRL, Via Cristoforo Colombo, 1, Torino, Italy, 10124.

<sup>2</sup>DET, Politecnico di Torino, Corso Duca degli Abruzzi, 24, Torino, Italy.

<sup>3</sup>Department of Neuroscience "Rita Levi Montalcini", Università degli Studi di Torino, Corso Massimo D'Azeglio, 52, Torino, Italy, 10126.

<sup>4</sup>AOU San Luigi Gonzaga, Università degli Studi di Torino, Regione Gonzole 10, Orbassano, Italy, 10043.

<sup>5</sup>Department of Orthopedic and Traumatology II - Hand Surgery Unit, CTO Hospital, Città della Salute e della Scienza, Via Gianfranco Zuretti 29, Torino, Italy, 10126.

<sup>6</sup>DIGEP, Politecnico di Torino, Corso Duca degli Abruzzi, 24, Torino, Italy.

<sup>7</sup>College of Science and Engineering, Hamad Bin Khalifa University, LAS Building, Doha, Qatar,.

<sup>8</sup>Neuroscience Institute Cavalieri Ottolenghi, Regione Gonzole 10, Orbassano (TO), Italy.

\*Corresponding author(s). E-mail(s): [corrado.cali@unito.it](mailto:corrado.cali@unito.it);

†These authors contributed equally to this work.

## Abstract

**Purpose:** *Minimally invasive surgery* (MIS) has emerged in clinical practice to minimize surgical trauma, providing patients with faster recovery, reduced pain and complications and enhanced aesthetic results compared to traditional surgery. However, this approach increase the risk of iatrogenic damage, i.e. the accidental injury to sensitive anatomical structures (eg. nerves and vascular structures) not directly visible during a percutaneous access. Augmented reality (AR) can effectively mitigate these drawbacks by overlaying graphical information onto the surgical field and providing real-time feedback, offering support in

training settings and clinical practice. Implementation challenges have limited the number of case studies in the scientific literature. This study presents a novel simulation paradigm for orthopedic surgery training, filling a gap in surgical skill development resources for trainees, and demonstrating the effectiveness of this approach.

**Methods:** The proposed methodology provides a framework for building a cost-effective and easily reproducible surgical training simulation environment. To address the challenge of mental spatial navigation during MIS procedures, the framework's rationale is to *address the challenge of mental spatial navigation during MIS procedures*. A surgical gesture tracking system using a commercial depth camera for comfortable simulation was developed. The principles of the acquisition system, image processing, and spatial computation mechanics are detailed to illustrate the framework's applicability. Digital environments customization with game engines to simulate expensive medical instrumentation, such as the C-arm, is also demonstrated. The simulation platform comprises a Computer Vision (CV) module, an X-ray machine simulation module, and an AR module.

**Results:** System validation involved analysis at different framework levels. From texture analysis of acquired images to application accuracy evaluation, the influence of various parameters on system performance is demonstrated. The simulation system is a valuable tool for learning minimally invasive procedures and for developers building AR systems for medical applications. The implementation is focused on the insertion surgical devices, including screws and K-wires. This is results in real application in minimizing the risk of iatrogenic injury to neural and vascular structures. To demonstrate the effectiveness of highly reproducible accuracy between real and virtual environment an analysis of errors and accuracies is illustrated at level of different subsystems. Measurement between comparative measurement between vernier caliper and simulation system methods shows a  $R > 0.9$  with a  $p < 0.01$ . Application accuracy was evaluated using the following parameters. The relative point-to-point accuracy averaged **1.02mm** with a standard deviation of **2.82mm**. Future development includes clinical implementation and integration of advanced AI technologies.

## 1 Introduction

Minimally invasive surgery (MIS) is associated with reduced postoperative pain and swelling, faster recovery times, a lower risk of complications, and the possibility of outpatient treatment [1]. Despite these benefits, MIS presents significant challenges. During surgery, hidden blood vessels and nerves are easily injured with potential long-term complications[2, 3]. Sharma et al. reported a 32.3% overall complication rate in pediatric upper limbs fractures treated with k-Wires, with wound complications and neurological impairments [4]. Besides, MIS relies on traditional X-rays that are associated with a risk of significant exposure morbidity [5]. In order to significantly reduce negative outcomes of percutaneous procedures leading to iatrogenic damage, deep knowledge of surgical anatomy coupled with surgical training is of the utmost importance. Within the last 15 years, Augmented Reality (AR) coupled to head mounted displays (HMDs) has emerged as a promising technology to enhance the accuracy and safety of surgical procedures[6, 7]. AR offers real-time visual insights

into anatomical structures, potentially reducing the risk of inadvertent injury[8, 9]. While AR may enhance minimally invasive orthopedic surgery (MIOS), its clinical adoption remains limited.

In MIOS the visualization of the patient’s internal anatomy is essential[10]. Discovered by Röntgen, X-rays enabled the development of the fluoroscope machines, the medical imaging gold standard for orthopedic surgical guidance [11]. In operating room, C-arms provide real-time dynamic radiographs, but expose patients and staff to radiation [12]. In the last 20 years, Surgical Navigation Systems (SNS) have become widespread in MIOS, guiding procedures on the hip [13], foot [14], tibia, spine [15, 16], and hand [17], as well as for the pelvis and sacral region [18]. The setup features a Dynamic Reference Frame (DRF) rigidly fixed to the patient for implicit volume registration. The imaging device is calibrated relative to the DRF using the known pose of the reconstructed volume[19]. These systems are highly effective for implanting screws and k-Wires in fracture reduction, arthrodesis, and osteotomies, enhancing surgical accuracy and safety. Specializing surgeons are trained in medical school for the use of intraoperative C-arm, as well as the interpretation of the 2D images. However, they still lack comprehensive 3D visualization for optimal guidance, for this reason the implementation of AR technology is a promising solution.

AR-Image Guide Systems offers improved visual guidance by providing real-time, 3D visualizations of anatomical structures [20]. These are particularly successful in neurosurgery, otolaryngology, maxillofacial surgery, and orthopedic surgery [21]. Clinically approved solutions, such as Medacta’s NextAR, are available for knee, shoulder, and spinal procedures, demonstrating significant potential in improving accuracy and outcomes in these areas [22, 23]. Despite these advancements, surgical trainees frequently lack convenient training environments and are exposed to X-rays during operating room practice [12]. Additionally, the existing systems are costly and specialized, hindering widespread distribution [24]. In this context, surgical simulation becomes essential for addressing these challenges, providing a safer and more accessible training alternative [25–28].

The introduction of head-mounted displays (HMDs), like the Microsoft HoloLens, has significantly advanced AR research in the clinical field [29]. In orthopedic surgery, studies using Microsoft HoloLens 2 have shown that AR systems can enhance surgical precision and outcomes, but its frameworks are not yet compatible with real surgical gestures [30]. Hajek et al. (2018) introduced an inside-out tracking paradigm with optical see-through head-mounted displays (OST HMDs), improving hand-eye coordination and accuracy in procedures such as C-arm-guided punctures [31]. Wang et al. (2019) developed an AR navigation system for minimally invasive total knee arthroplasty, significantly reducing radiation exposure by eliminating the need for intraoperative X-ray imaging [32]. Gsaxner et al. (2021) presented an inside-out instrument tracking system using the HoloLens 2’s built-in stereo cameras, achieving clinically relevant localization accuracy for surgical instruments [30]. Cutolo et al. (2020) designed a highly configurable software framework for AR applications in

surgery, demonstrating sub-millimeter precision in guiding surgical incisions [33]. Hu et al. (2022) developed a markerless orthopedic navigation platform with reliable AR overlay accuracy, showcasing its potential to enhance the ergonomics and efficiency of computer-assisted orthopedic surgery (CAOS) [34].

We introduce a novel augmented reality simulation framework for the accurate implantation of k-Wires in a 3D-printed elbow phantom. This integration allows to visualize and accurately place k-Wires in strategic positions, ensuring a high degree of precision and reducing the risk of complications. This article will provide a detailed description of the developed AR system and the methods used to evaluate its effectiveness, compared to the traditional approach using the C-Arm. We propose our simulator as an effective, low-cost training tool for specializing surgeons. Finally, the conclusions and implications of this study for clinical practice will be presented. Table 2 presents relevant works for comparison with ours. These studies primarily focus on orthopedic surgery, as they involve rigid bodies and avoid the challenges of soft tissue deformation. For comprehensive reviews of the current state of augmented reality in surgical applications, see Ma et al. [35] and Ulrich et al. [36]. Addressing soft tissue deformation would require a more complex model, which is often unsuitable for current computational platforms. There is also a lack of uniformity in the methods used to determine system accuracy among these studies. Currently, there is no standardized methodology to assess how errors and uncertainties affect the various steps of the process. Furthermore, accuracy is defined at different levels by researchers and instrument manufacturers.

Article	Accuracy/Error	AR technology
Development of a surgical navigation system based on augmented reality using an optical see-through head-mounted display (2015) [37]	$E_{RMS} = 0.809mm$	HDM (Hololens 2)
Inside-Out Instrument Tracking for Surgical Navigation in Augmented Reality (2021) [38]	$E_{RMS} = 1.70mm$	HDM (Hololens 2)
Augmented reality navigation for precise implantation of LC2 pelvic tunnel screws in minimally invasive surgery (2024) [39]	$E_{RMS} \approx 1mm$	HDM - external tracking system
STTAR: Surgical Tool Tracking Using Off-the-Shelf Augmented Reality Head-Mounted Displays (2024) [40]	lateral translation $\rightarrow$ $0.09 \pm 0.06mm$ longitudinal translation $\rightarrow$ $0.42 \pm 0.32mm$	HDM (Hololens 2)

**Table 1:** Similar Works

## 2 Material and Methods

The framework, designed for accessibility and adaptability, facilitates training and research within MIOS. The developed platform simulates a realistic surgical environment for AR-assisted procedures replicating essential components. This framework through Microsoft’s HoloLens 2 provide a real-time surgical guidance, supporting the simulated C-arm ones. The integration purpose is to enhance accuracy and efficiency of the procedure.

### 2.1 Framework Rationale

Augmented reality has the potential to efficiently inform surgeons and physicians for intervention planning and real-time support, speeding up intervention time and reducing healthcare system costs. The rationale behind this framework is to *“provide the right information in the most suitable form”*. Using digital anatomical atlases makes it possible to achieve the highest coherency between real-world and digital information. Practitioners can study the anatomy of a digital model before a procedure and then verify their understanding with 3D visual information and haptics during the intervention. Although physiological anatomy contains many variables that require continuous monitoring for procedure execution, in the training phase, using simplified systems can help practitioners better understand the relationship between anatomy (real-world information) and the task at hand, thus speeding up the learning process. In fact, the introduction of computer-based interventional medicine has enabled the combination of information from many sources. However, this has sometimes caused a lack of real correspondence to the operator’s view of the body they are working on.

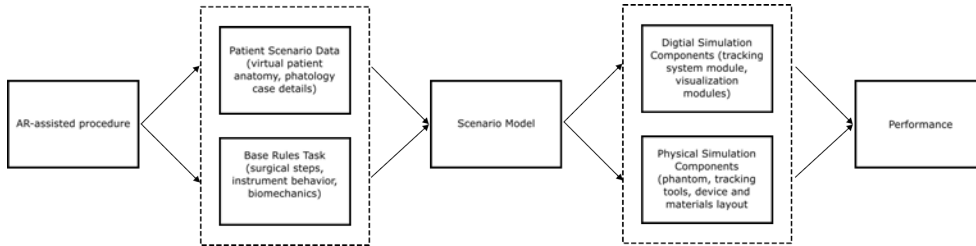


**Fig. 1:** Framework components.

Figure 1 illustrates the core components of the framework for AR-assisted surgical simulation. The process begins with the question: *Which AR-assisted procedures should be simulated?* This question establishes the simulation’s context, encompassing surgical task rules and patient case study contextualization. The virtual patient is defined by anatomy, pathology, and other relevant details. Digital atlases, such as z-Anatomy (CC BY-SA 4.0), provide patient data. The *Scenario Model* requires both patient data and task rules (e.g., surgical steps, instrument behavior, biomechanics). Surgical steps define instrument and personnel interaction within the model. Scenario

Tools	Function
Blender	Modelling (non parametric). Organic shapes with sculpting tools
Fusion 360	Modelling (parametric). Dimension-driven 3D models
Sketch Fab	3D Model Store
z-Anatomy	Anatomy Navigable Atlas
Unity	Game Engine. Create environments and simulate realistic physics interaction
MRTK for Unity	Mixed Reality Development. Framework for Mixed Reality experience in Unity

**Table 2:** Framework development Tools

construction utilizes digital and physical simulations. The digital component necessitates a *computer-integrated intervention medicine* architecture. Game engines, such as Unity, facilitate medical informatics platform simulation. These platforms enable data integration and realistic surgical simulations. Table 1 report a useful tools for workflow development.

## 2.2 System Overview

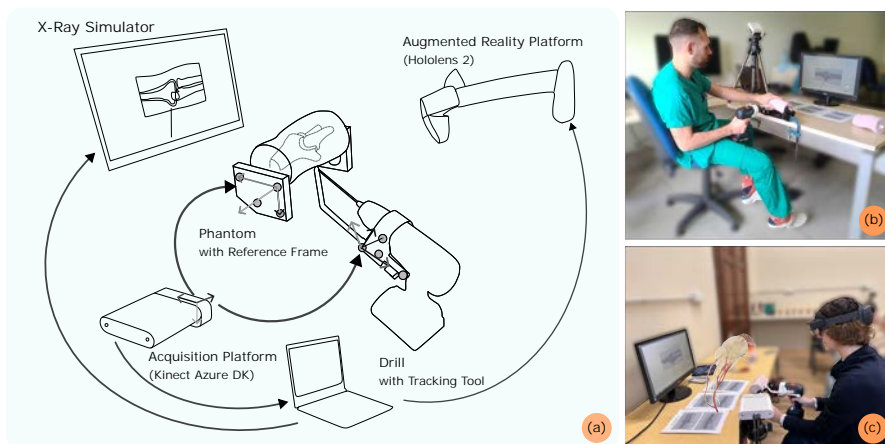


**Fig. 2:** Experimental setup for simulating and evaluating an AR-guided surgical procedure. (a) The schematic shows the system components: X-ray simulator, Kinect Azure DK for motion tracking, a phantom with a reference frame, and a Hololens 2 headset for AR guidance. Two operational modalities. (b) X-ray-guided procedure without AR. (c) AR-guided procedure using the Hololens 2.

The modular architecture of the system integrates multiple hardware and software platforms (Figure 2). A *Kinect Azure DK* depth camera captures real-time depth map data, enabling tracking and visualization of IR-marked surgical tools for pose estimation. The workstation, equipped with Windows 10 OS, a 64-bit Intel(R) Core(TM) i7-9750H CPU, and an Nvidia RTX 2080 GPU with Max-Q Design, runs both the Unity<sup>1</sup>-based c-Arm simulation software and the AR navigation system. A

<sup>1</sup><https://unity.com/>

*Hololens 2* serves as HMD platform for AR visualization.

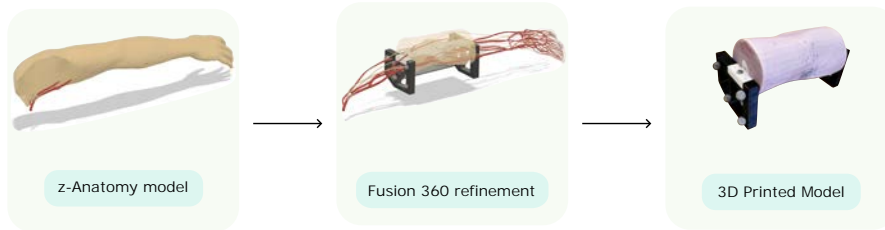


**Fig. 3:** Development pipeline for the 3D printed phantom. A z-Anatomy digital model was used as the initial template. This template was refined for printability and feature integration using Fusion 360 CAD software. The resulting design was then 3D printed to produce the physical phantom.

The elbow’s anatomical model, derived from the z-Anatomy atlas, was integrated with tracking tool designs within Autodesk Fusion 360, utilizing .fbx files exported from Blender (Figure 3). This integration enabled the study of vascular and nerve damage relative to target points positioned on the physical dummy. A complementary mold facilitated the accurate positioning of 3D-printed PLA radius, ulna, and humerus sections, replicating the digital elbow model physically. Figure 4 illustrates the digital and real models of the tracking tools.

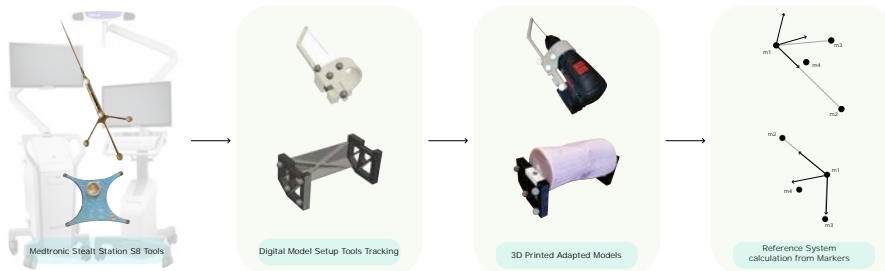


**Fig. 4:** Development of custom tools inspired by Medtronic Stealth Station S8 tools. The process includes: adapting Medtronic S8 tools for our setup, creating corresponding digital models, 3D printing the adapted models, and establishing a reference system using marker calculations.

Figure 5 illustrates the data workflow feeding the simulation platforms. The *Kinect Azure DK* captures raw IR camera data and depth map. These data is inputs of the *Tracking System* and processed to extract the coordinates of spherical markers. The *X-Ray Simulator and AR Guidance System* elaborate these for the simulation and augmented reality guidance. The *system workflow*, inspired by surgical navigation

systems [32], comprises three main steps (calibration, alignment, and visualization). It is designed to facilitate k-Wire placement through the integration of optical tracking and AR. In the *calibration* step the holographic space is calibrated within the AR environment. Multiple marker sphere position are collected to solve the *transformation matrix*, aligning the holographic space with the physical space. This alignment is crucial for ensuring accurate AR guidance during the simulation. In the *alignment* step virtual models are aligned with the physical space of phantom models. The final step involves the real-time *visualization* of digital content through the AR system (HoloLens 2) onto the real-world surgical field.

## 2.3 Tracking System Module

Near Infrared Optical Tracking Systems (NIOTS) are widely used in clinical settings. They excel at accurately estimate the pose of anatomical structures or instruments. Operating in the near-infrared spectrum, the interference from ambient light is minimized [30, 41]. NIOTS can be active or passive. Active systems use IR LEDs on the tracked object, while passive systems employ IR LEDs on the camera to illuminate retroreflective markers. Spherical markers are often preferred in passive systems as they efficiently reflect light back to the source. Optical tracking necessitates at least three non-collinear markers on the object, to determine an object’s 3D pose. Tracking system module is based on these principles and illustrated in the following section.

### 2.3.1 Acquisition Platform

The proposed framework is based on an marker based *outside-in approach*. As depicted in Figure 6 this involves the use of external sensors that surround objects, enabling to track movements from the outside. Affordable commercial and open-source alternatives to clinically approved systems exist for signal sources and sensor platforms. HoloLens 2 and Azure Kinect DK are equipped with the same depth camera module [42]. Gsaxner et al.[30] demonstrated the feasibility of an *Inside-Out approach based system* using the HoloLens 2 integrated sensors. However, as illustrated in Figure 6 this approach was deemed unsuitable for our framework due to the device limited and head position dependent field of view in the surgical setting. Moreover, the insufficient temporal stability observed in the infrared (IR) marker coordinates provided by the sensors resulted in a lack of smooth virtual tool motion, which is essential for realistic surgical simulation. To address this issue, an approach involving external cameras has been investigated.

*Kinect Azure DK* and *Intel RealSense 435i* cameras have been considered viable options as external acquisition sources. Figure 7 illustrates their differing IR frame and depth map acquisition, while Table 3 resume main technical characteristics. The Kinect Azure DK was selected for its Continuous Wave Time of Flight (CW-ToF) depth camera and wider field of view. This to achieve high performance on marker tracking for surgical procedures. In contrast, Intel RealSense cannot selectively acquire light from markers since structured light based hardware. In [45] is reported a systematic comparison of these devices. The Azure Kinect offers superior accuracy at long range and a wider field of view.

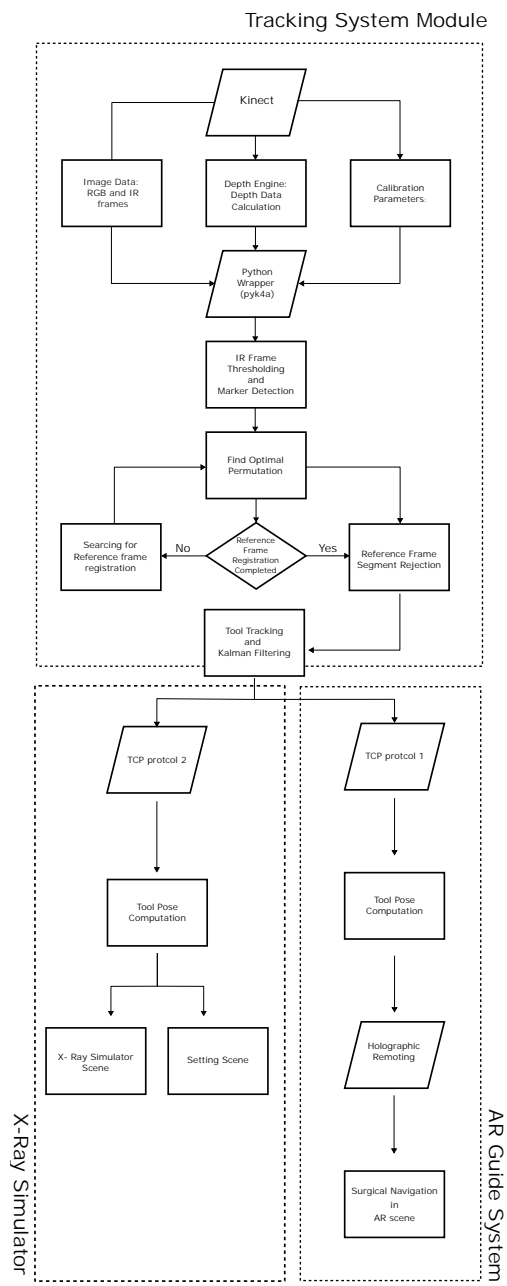


**Fig. 5:** Data processing workflow

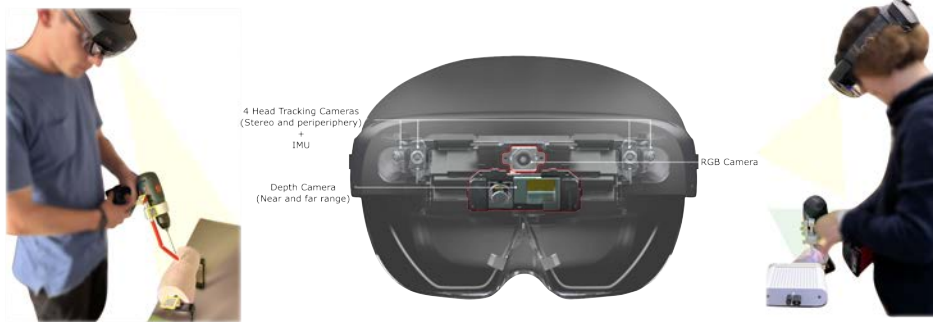


**Fig. 6:** At the center Hololens 2. The Depth Camera Module is marked in red. Two operating modes are compared. QR code-based tracking uses the RGB camera. IR marker-based tracking uses the Depth Camera. QR code processing is computationally expensive. IR markers are susceptible to occlusion. Kinect Azure DK tracking is compatible with surgical gestures.

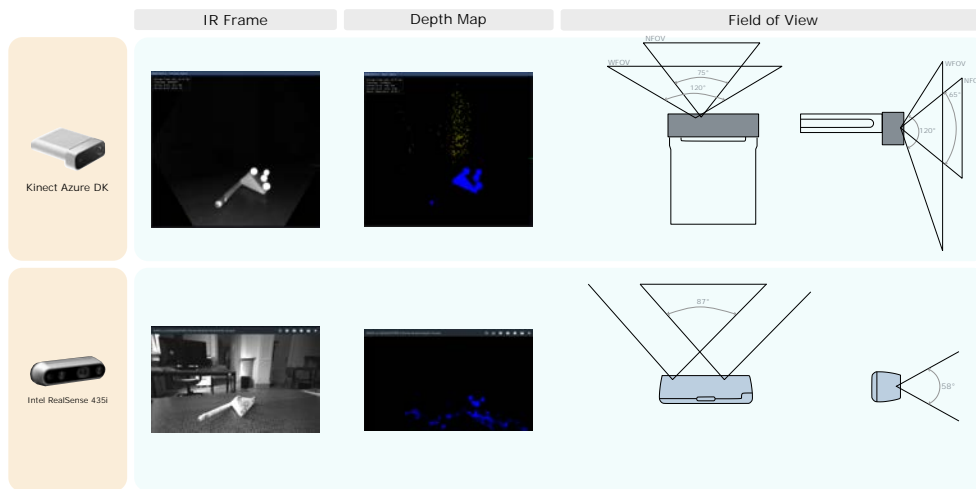


**Fig. 7:** Kinect Azure DK and Intel RealSense 435i depth-sensing cameras performance comparison. The figure illustrates the infrared (IR) frame, depth map, and field of view (FOV) for each camera. The Kinect Azure DK has a wider FOV ( $120^\circ$ ) compared to the Intel RealSense 435i ( $87^\circ$  horizontally,  $58^\circ$  vertically).

**Table 3:** Kinect Azure DK and Intel RealSense D435i comparison

Category	Kinect Azure DK [43]	Intel RS D435i [44]
Depth Technology	Time of Flight	Stereoscopic
Depth Field of View	$75^\circ \times 65^\circ$ (NFOV), $120^\circ \times 120^\circ$ (WFOV)	$87^\circ \times 87^\circ$
Depth Frame Rate	Up to 30 fps	Up to 90 fps
Resolution	512x512	1280 × 720
Depth Range	0.5 - 5.46m (depending on mode)	0.3 m - 3 m

### Camera Setting

Continuous Wave ToF cameras measure distance by cross-correlating emitted and reflected amplitude-modulated light. The Azure Kinect DK incorporates a 1-Megapixel Time-of-Flight (ToF) depth camera (Figure 8). This camera’s sensor features high modulation contrast at high frequencies (87% at 200MHz, 78% at 320MHz), small pixel size ( $3.5\mu\text{m} \times 3.5\mu\text{m}$ ), and an efficient clock driver system enabling up to 320MHz modulation [46]. It has four Field of View depth acquisition mode: binned and unbinned narrow field-of-view (NFOV) and wide field-of-view (WFOV). Binning increases depth range combining adjacent sensor pixels into a bin. The NFOV depth camera’s illuminator has no tilt, while WFOV illuminator is tilted down of 1.3 degrees [47].

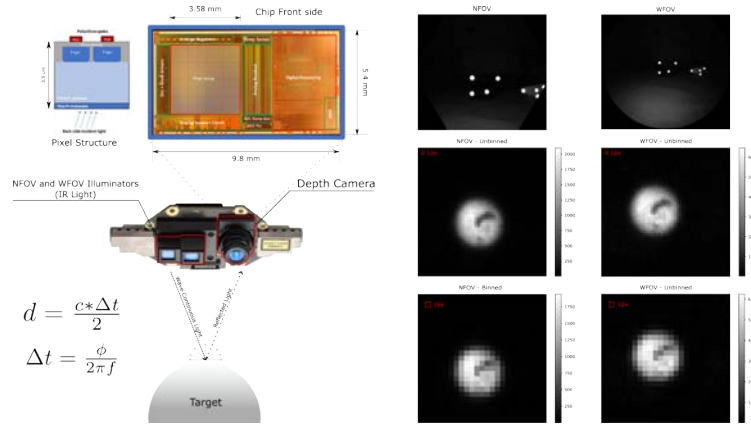


**Fig. 8:** The Kinect sensor’s operating principle is shown on the left. Its 1Mpixel 65nm BSI 320MHz Demodulated TOF Image Sensor uses  $3.5\mu\text{m}$  global shutter pixels and analog binning in a  $1024 \times 1024$  array. The photodetector has a polysilicon gate PGA and PGB. On the right, four acquisition mode ROIs are compared. NFOV images have higher gray values, while binned images reduce resolution for better depth measurement.

### Camera Performance

The Influence of Camera Distance on performance can be assessed using systematic and random errors. *Systematic error* is the difference between the average measured depth (after noise reduction) and the ground truth depth. It’s calculated as:

$$E_{systematic} = \frac{\sum_{t=1}^N d_t}{N} - d_{gt} \quad (1)$$

where  $d_t$  denotes the measured depth at time  $t$ ,  $N$  is the number of frames used in the averaging, and  $d_{gt}$  is the ground truth depth. *Random error*, caused by variations in

photon counts (shot noise), is defined as the standard deviation of depth measurements over time in a static scene. It's calculated as:

$$E_{random} = \sqrt{\frac{\sum_{t=1}^N (d_t - \bar{d})^2}{N}} \quad (2)$$

where  $N$  denotes the number of depth measurements,  $d_t$  represents the depth measurement at time  $t$ , and  $\bar{d}$  denotes the mean value computed over all depth measurements  $d_t$  [48].



**Fig. 9:** Systematic and Random Error Setup Measurement

To evaluate the depth sensor measurement accuracy, an experiment was designed using Kinect Azure mounted on a camera tripod and a sheet of graph paper on a parallel support. Distances between these components were set at 0.5 m and 1 m, representing typical and maximum operational distances. A laser rangefinder was used to measure the distance between the two components. Depth measurements were limited to these distances. The captured depth image was cropped, using only the region of interest for measurements at the point indicated by the laser rangefinder.

### *Depth Engine Performance*

Depth engine converts raw sensor data into a normalized depth map. The depth engine code is proprietary to the Azure Kinect DK hardware [49]. To evaluate its performance in information conversion first order texture parameters are involved. Texture is a function of spatial variation in pixel values. First-order statistics are calculated from the probability of a pixel having a specific value at a random location according the definition of histogram [50]. Evaluating these features in a large amount of frame it is possible understand the statistic device stability.

$$H(g) = \frac{n_g}{N}; g = 0, 1, \dots, G - 1 \quad (3)$$

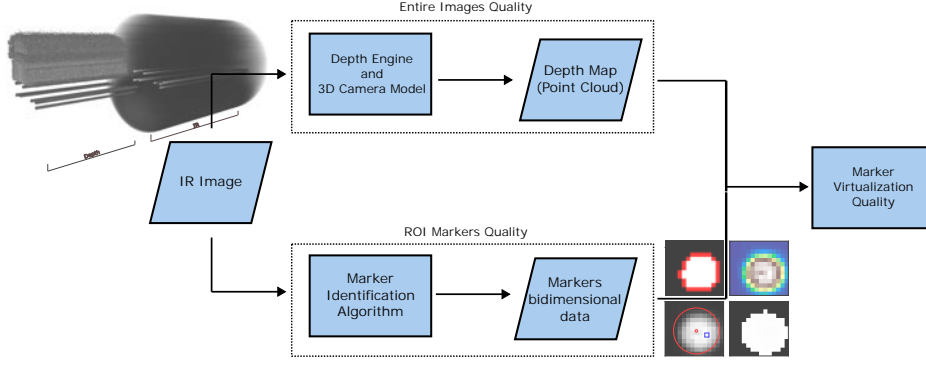


**Fig. 10:** Influence of Image Data features on Marker Virtualization Quality

Mean ( $P_1$ ), Standard Deviation ( $P_2$ ), Skew ( $P_3$ ) and Entropy ( $P_4$ ) are defined as follow:

$$P_1 = \sum_{g=0}^{G-1} gH(g) \quad P_2 = \sqrt{\sum_{g=0}^{G-1} (g - P_1)^2 H(g)} \quad (4)$$

$$P_3 = \frac{\sum_{g=0}^{G-1} (g - P_1)^3 H(g)}{P_2^3} \quad P_4 = - \sum_{g=0}^{G-1} H(g) \log_2(H(g)) \quad (5)$$

Signal metrics assess sensor performance. The mean shows average signal level. Shifts over time suggest drift, illumination changes, or systematic issues. Standard deviation measures signal variability. High values may indicate noise, unstable lighting, or vibration. Low values may suggest lost detail or limited dynamic range. Skew reflects signal distribution asymmetry. Changes can reveal shifts, potentially indicating non-linear response or biases. Entropy measures signal information. Decreases may suggest information loss or reduced complexity. Increases might indicate higher noise or unpredictable elements.

### 2.3.2 Image Processing

The Kinect Azure DK sensor, configured in wide field of view (WFOV) mode, captured infrared (IR) and depth images. Reflective markers were segmented from the IR images using an intensity threshold and Circle Hough Transform (CHT), with centroids calculated from 3D cloud points. Correspondences were established via Procrustean analysis, comparing the target frame pattern with coordinate set permutations. The 3D coordinates of tracked tool markers were sent to X-Ray Simulation Software and AR guide systems via UDP. As can be seen in Figure 11, the Graphical User Interface (GUI), HoloElbow-ComputerVisionModule, centrally displays the infrared image, depth map, processed IR image, and RGB image, with controls for resetting coordinates, stopping tracking, saving data, and selecting the tracked tool. The open-source HoloElbow-ComputerVisionModule framework, is accessible on GitHub<sup>2</sup>.

<sup>2</sup><https://github.com/Antocg99/01-HoloElbow-ComputerVisionModule>

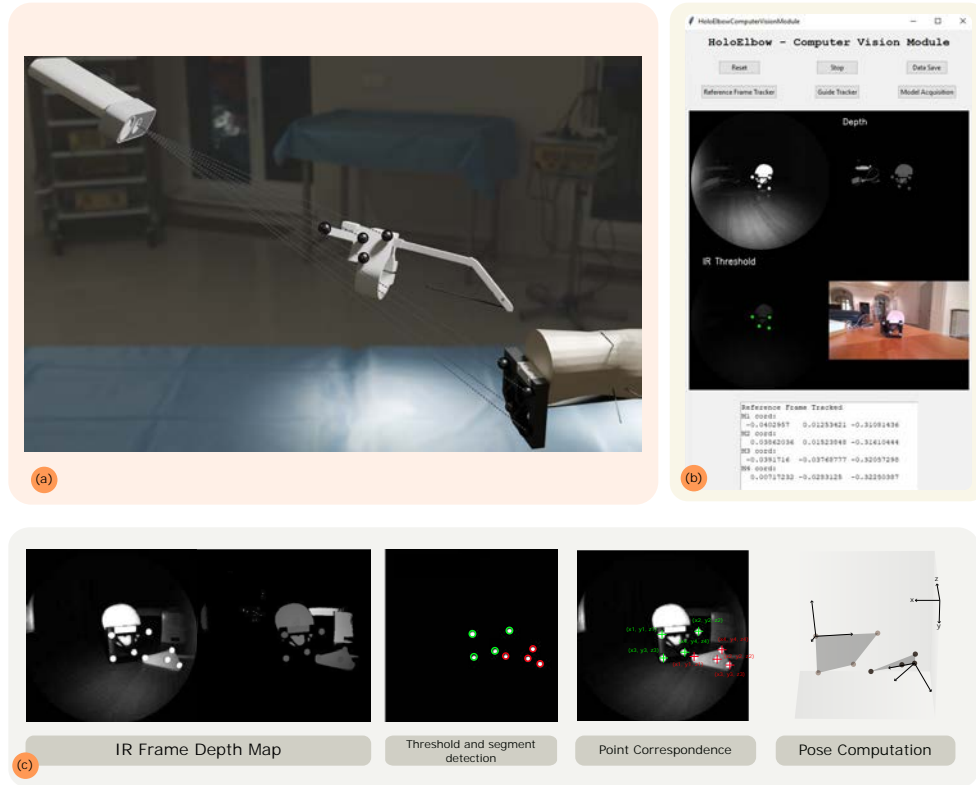


Fig. 11: Computer Vision Module

### 2.3.3 Space Computation

In Kinect Azure DK each camera (depth and color) has a 2D coordinate system. Pixel coordinates range from  $[0,0]$  (top-left) to  $[\text{width}-1, \text{height}-1]$ , determined by the camera's mode. The 3D origin  $[0,0,0]$  is the camera's focal point. X-axis is positive right, Y-axis positive down, Z-axis positive [51]. Establishing reference coordinate systems in both physical and virtual environments is essential for accurate data alignment and effective task execution. In our system the following local reference coordinate systems are defined within the World Coordinate System (WCS): Patient Reference Coordinate System, Tracking Tool Coordinate System and Virtual Models Coordinate System. This section describes the computational methods used to determine element pose within the scene. These include the Pinhole Camera Model, lens distortion correction, and fiducial point-based registration. A model for calculating error within the spatial transformation matrix is also provided.

#### *Pinhole Camera Model*

The WCS is camera-dependent. Kinect origin is the focal point, with the  $x$ -axis pointing right, the  $y$ -axis down, and the  $z$ -axis forward (to review the notation). Pine-Hole

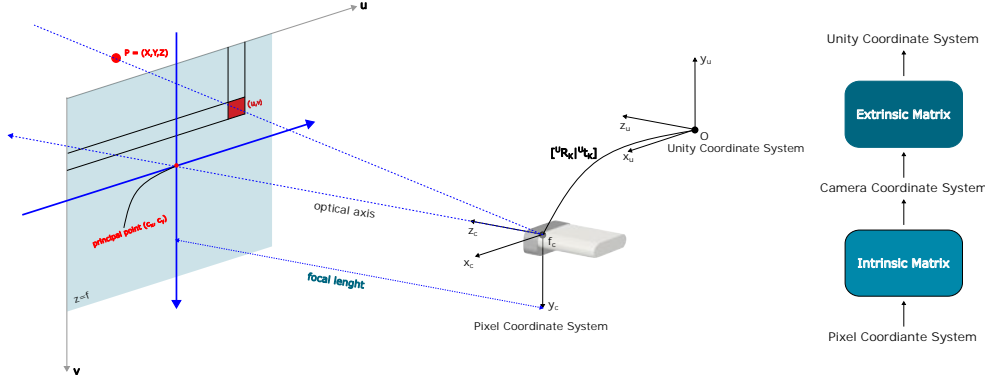


**Fig. 12:** Kinect has a right-handed coordinate system. Unity has a left-handed coordinate system

camera model describe the spatial relationship between real world and camera space. Equation 6 describe the relationship between image plane and 3D coordinate system.

$$d \begin{bmatrix} u \\ v \\ 1 \end{bmatrix} = \underbrace{\begin{bmatrix} f_x & 0 & c_x \\ 0 & f_y & c_y \\ 0 & 0 & 1 \end{bmatrix}}_{\text{intrinsic matrix}} \underbrace{\begin{bmatrix} r_{11} & r_{12} & r_{13} & t_1 \\ r_{21} & r_{22} & r_{23} & t_2 \\ r_{31} & r_{32} & r_{33} & t_3 \end{bmatrix}}_{\text{extrinsic matrix}} \begin{bmatrix} x_w \\ y_w \\ z_w \\ 1 \end{bmatrix} = \mathbf{K}[\mathbf{R}|\mathbf{t}] \begin{bmatrix} x_w \\ y_w \\ z_w \\ 1 \end{bmatrix} = \mathbf{M} \begin{bmatrix} x_w \\ y_w \\ z_w \\ 1 \end{bmatrix} \quad (6)$$

Since no rotation neither translation is applied, this results in a identity extrinsic matrix  $M$ . The homogeneous 3D point  $P$  results in the same 3D point:

$$\begin{bmatrix} x_c \\ y_c \\ z_c \end{bmatrix} = \mathbf{K}^{-1} \begin{bmatrix} u \\ v \\ 1 \end{bmatrix} = \begin{bmatrix} \frac{1}{f_x} & 0 & -\frac{1}{c_x} \\ 0 & \frac{1}{f_y} & -\frac{1}{c_y} \\ 0 & 0 & 1 \end{bmatrix} \begin{bmatrix} u \\ v \\ 1 \end{bmatrix} d = \begin{bmatrix} \frac{u-c_x}{f_x} d \\ \frac{v-c_y}{f_y} d \\ d \end{bmatrix} \quad (7)$$

Unity uses a left-handed coordinate system [52], while Kinect Azure DK 3D system is right-handed [51]. To convert coordinate points is applied a transformation matrix with for z-coordinate reflection.

$$\mathbf{p}_U = \begin{matrix} K \\ U \end{matrix} \mathbf{T} \mathbf{p}_K = \begin{bmatrix} \begin{matrix} K \\ U \end{matrix} \mathbf{R} & \begin{matrix} K \\ U \end{matrix} \mathbf{t} \\ 0 & 1 \end{bmatrix} \mathbf{p}_K = \begin{bmatrix} 1 & 0 & 0 & 0 \\ 0 & 1 & 0 & 0 \\ 0 & 0 & -1 & 0 \\ 0 & 0 & 0 & 1 \end{bmatrix} \mathbf{p}_K$$

### *Spatial Transformation Matrix*

In Image Guided Therapy the accuracy of the treatment depends on 3D spatial error. Transformations between associated coordinate systems depends on function

${}^A_B\mathbf{T}$  describing the relationship between two coordinates of the same point [53].

$$\tilde{\mathbf{v}}_B = {}^A_B\mathbf{T}(\tilde{\mathbf{v}}_A) = {}^A_B\mathbf{R} \cdot \tilde{\mathbf{v}}_A + {}^A_B\tilde{\mathbf{p}} \quad (8)$$

Equation 8 relate coordinate  $\tilde{\mathbf{v}}_A = [x_A, y_A, z_A]$  to  $\tilde{\mathbf{v}}_B = [x_B, y_B, z_B]$  through a rotation  ${}^A_B\mathbf{R}$  and a translation  ${}^A_B\tilde{\mathbf{p}}$ .  ${}^A_B\mathbf{R}$  is representable by a rotational motion with an angle  $\theta$  around an axis  $\hat{\mathbf{n}}$ .

$${}^A_B\mathbf{R}(\mathbf{n}, \theta) = e^{\theta \hat{\mathbf{n}}} \quad \text{where} \quad \hat{\mathbf{n}} = \begin{bmatrix} 0 & -n_z & n_y \\ n_z & 0 & -n_x \\ -n_y & n_x & 0 \end{bmatrix}. \quad (9)$$

The ideal transformation ( ${}^A_B\mathbf{T}$ ) is related to real ones ( ${}^A_B\tilde{\mathbf{T}}$ ) by a perturbation ( $\Delta_B^A\mathbf{T}$ ):

$${}^A_B\tilde{\mathbf{T}} = {}^A_B\mathbf{T} \cdot \Delta_B^A\mathbf{T} \quad (10)$$

The rotational component of  $\Delta_B^A\mathbf{T}$  is described by a first-order Taylor series approximation, so small rotations have negligible effects.

$$\Delta_B^A\mathbf{R}_{\text{Rot}} \approx \mathbf{I} + \theta \mathbf{N}, \quad (11)$$

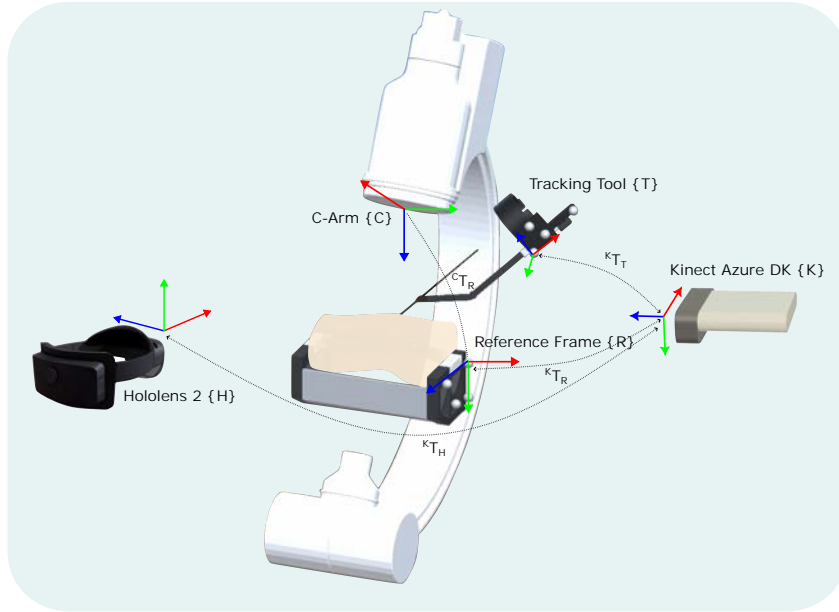


**Fig. 13:** Transformation relationship between components. Global reference system is associated with Unity Space.

### *Lens Distorsion Correction*

Lens system introduce optical distortion in depth maps. This is formulated with Brown–Conrady model with radial and tangential distortion terms. Undistorted pixel coordinates are obtained through reverse mapping from the observed (distorted) pixel values.

$$x_d = \frac{1 + k_1 r^2 + k_2 r^4 + k_3 r^6}{1 + k_4 r^2 + k_5 r^4 + k_6 r^6} x + 2p_1 xy + p_2(r^2 + 2x^2) \quad (12)$$

$$y_d = \frac{1 + k_1 r^2 + k_2 r^4 + k_3 r^6}{1 + k_4 r^2 + k_5 r^4 + k_6 r^6} y + 2p_2 xy + p_1(r^2 + 2y^2) \quad (13)$$

### *Fiducial-Based Registration*

Local reference systems are calculated using the non-collinear positions of Kinect-tracked spherical markers. Considering  $\mathbf{P}_1(p_{1x}, p_{1y}, p_{1z})$ ,  $\mathbf{P}_2(p_{2x}, p_{2y}, p_{2z})$ ,  $\mathbf{P}_3(p_{3x}, p_{3y}, p_{3z})$  the coordinate position of fiducials, the *normal vector*  $\vec{n}$  to the plane defined by the points is defined as in Equation 14.

$$\vec{n} = \langle p_{3x} - p_{2x}, p_{3y} - p_{2y}, p_{3z} - p_{2z} \rangle \times \langle p_{3x} - p_{1x}, p_{3y} - p_{1y}, p_{3z} - p_{1z} \rangle \quad (14)$$

The  $x$ -axis is the normalized direction from  $x_3$  to  $x_2$ . The  $z$ -axis is the normalized cross product of  $\vec{x}$  and  $\vec{v}_{\text{sup}}$ . The  $z$ -axis is defined as the cross product of the  $x$ -axis and the plane normal derived from the three markers.

$$\hat{\mathbf{x}} = \frac{\langle p_{3x} - p_{2x}, p_{3y} - p_{2y}, p_{3z} - p_{2z} \rangle}{\|\langle p_{3x} - p_{2x}, p_{3y} - p_{2y}, p_{3z} - p_{2z} \rangle\|} \quad \hat{\mathbf{y}} = \frac{\hat{\mathbf{x}} \times \vec{n}}{\|\hat{\mathbf{x}} \times \vec{n}\|} \quad \hat{\mathbf{z}} = \hat{\mathbf{x}} \times \hat{\mathbf{y}} \quad (15)$$

$\hat{x}$ ,  $\hat{y}$ , and  $\hat{z}$  form an orthonormal basis for the local reference frame centered at  $P_1$ . The corresponding 4x4 homogeneous transformation matrix (relative to the global frame) is:

$$\mathbf{T} = \begin{bmatrix} \hat{x}_x & \hat{y}_x & \hat{z}_x & p_{1x} \\ \hat{x}_y & \hat{y}_y & \hat{z}_y & p_{1y} \\ \hat{x}_z & \hat{y}_z & \hat{z}_z & p_{1z} \\ 0 & 0 & 0 & 1 \end{bmatrix} = \begin{bmatrix} \mathbf{R} & \mathbf{p} \\ 0 & 1 \end{bmatrix} \quad (16)$$

## 2.4 Visualization Modules

Developed system is composed by two visualization platform. User is provided by a X-Ray simulator and an AR Guide System. The first ones simulate the C-Arm machine, while the second ones is the implementation of Augmented Reality in the simulation environment. As can be seen in Figure 14 both submodules can be used at the same time. Stereoscopic rendering provides one depth cues, while X-Ray simulator give a 2D rendering. The first AR guided system can be explorable through head movement, while X-Ray Simulator through a pedalboard permit to change point of view as in operating room.

### *X-Ray Simulator*

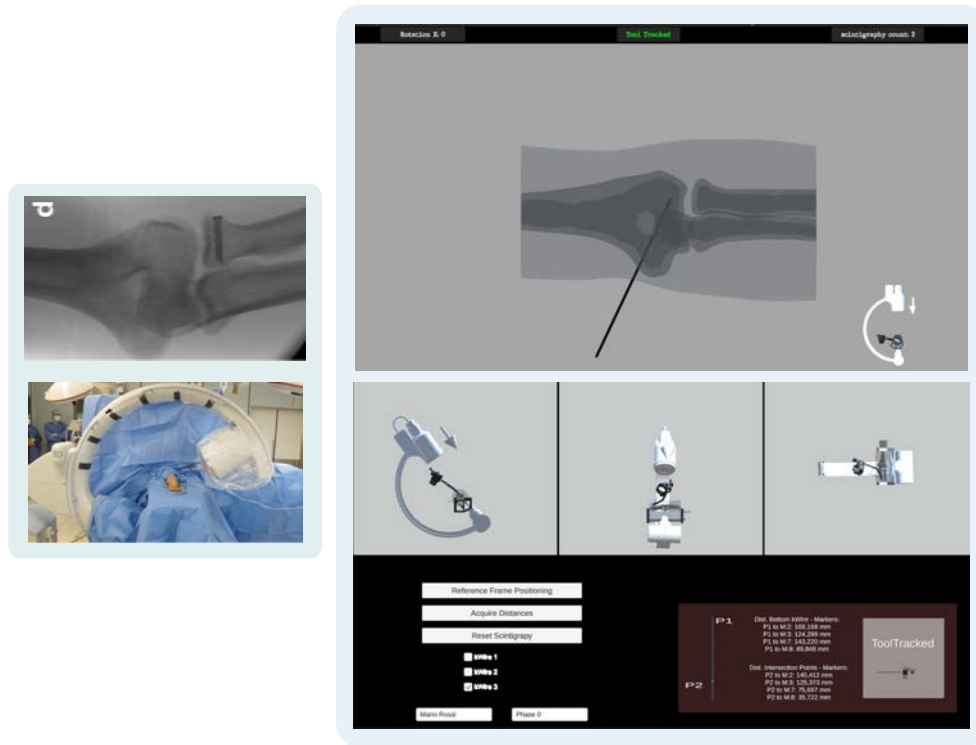


Fig. 14: A comparison between real C-Arm scenario[54] and simulated ones

The X-ray emulator simulates fluoroscopic imaging of a patient's elbow. The elbow model, extracted from the z-Anatomy atlas [55], was adapted and refined using Fusion 360<sup>3</sup>. This model, positioned within a simulated c-Arm environment, replicates X-Ray attenuation characteristics. The simulated c-Arm's interface replicates the key features and functionalities of a real operating room Fluoroscope Machine. It provides

<sup>3</sup>[www.autodesk.com/products/fusion-360](http://www.autodesk.com/products/fusion-360)

additional information including X-ray exposure count, tool tracking status and angulation. Additionally, a graphical representations of guiding elements and phantom aids in assessing relative positioning.

### *AR Guide System*

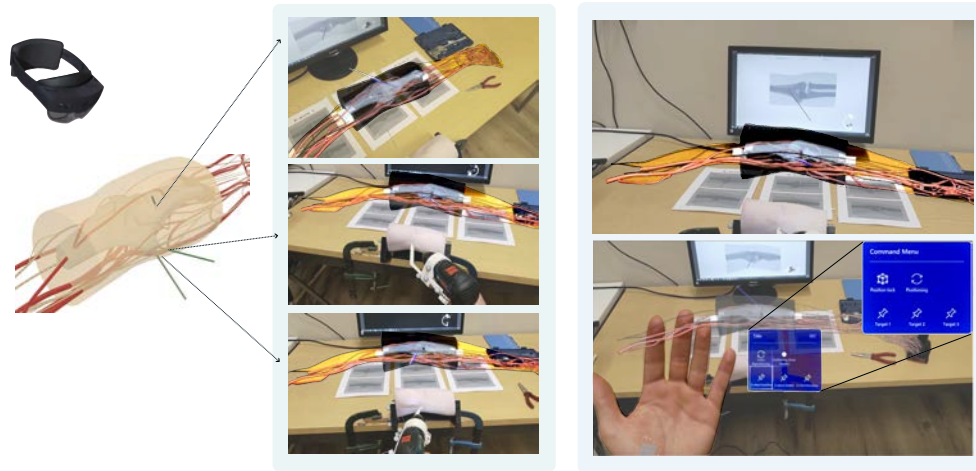


**Fig. 15:** AR Interface with Holographic Elbow. Images are recorded with Mixed reality Capture with a first-point of view. Original resolution is of 1920x1080 px, while frame rate is halved to 30Hz.

The AR Guide System is developed using the Mixed Reality Toolkit (MRTK) for Unity. Runtime code is written in C++, with development scripting in C#. MRTK automatically configures Unity for Mixed Reality development. Spatial coordinate systems are real-world coordinate systems used to define geometry. The headset's position is the center of the holographic world and is managed automatically by the Unity Camera for stereoscopic rendering. Holographic rendering in HoloLens 2 is achieved through a see-through display. White pixels are translucent, allowing light from the display to combine with light from the real world. Black pixels are fully transparent. Brighter pixels are increasingly opaque. HoloLens 2 defaults to a maximum render target resolution of 1440x936, but this can be scaled down to reduce GPU memory usage. A well-defined environment and optimized application development contribute to high-quality holograms. These holograms are synchronized with their corresponding real-world coordinates when the application runs constantly at 60 frames per second. This synchronization is maintained in environments where HoloLens can track its surroundings. Stationary holograms remain fixed in the environment, which is crucial for a positive user experience, especially in tasks requiring accuracy and precision.

In this scenario, through a HoloLens 2 virtual the anatomical models is projected onto the simulated surgical field. To ensure accurate real-world visualization, these models are not overlaid directly onto the physical model. The HMD's 3D visualization

enhances spatial awareness and provides an intuitive understanding of the surgical anatomy. Furthermore, critical nerve and vessel locations are displayed in the field of view, aiding navigation and decision-making to reduce complication risk. The HMD allows manipulation of virtual models, enabling to explore the anatomy, simulate surgical approaches and plan procedures. This AR application, developed with the Mixed Reality Toolkit (MRTK)[56], provides cross-platform input and spatial interaction. It runs locally in Unity Play Mode on a PC and is streamed to the HoloLens 2 via Wi-Fi.

The interface, depicted in Figure 15, is designed to facilitate the use of the AR application. Its touchless interaction is advantageous in both surgical settings, where it maintains sterility, and training environments, where it familiarizes users with hand-interface interaction. Virtual model registration is initiated with the *Positioning* button. Following registration within the 3D X-ray simulator space, the anatomical model can be further manipulated in the AR space. The *Position Lock* icon enables this functionality. The *Target X* buttons toggle the visualization of implant target trajectories on the virtual model, determined during planning simulations.

## 2.5 System Performance

Several components have been described in the previous paragraph. Assessing system performance requires a deep analysis at each level. However, due to the complexity of articulated systems, there is no standardized method for assessing IGS systems. To address this, we evaluate performance at two levels: superimposition error for the tracking system, and an ASTM-based evaluation for the system’s use for its intended purpose.

### 2.5.1 Application Accuracy

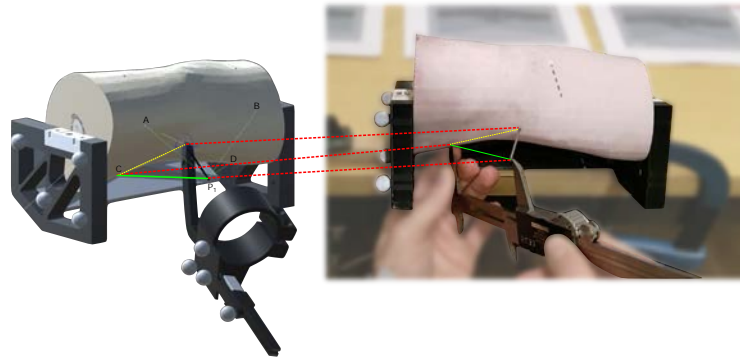


**Fig. 16:** Application Accuracy. In figure is illustrated how the same distance is acquired from the simulated navigation system and with a vernier caliper.

Application accuracy is defined, briefly, as the difference between the real position of given point in a 3D space, and the same position evaluated by the tracking system.

It was evaluated through a set of Kirschner wire (k-wire) implantation trials in three predefined positions within a simulation phantom containing ten markers distributed on the surface of the soft component (skin). The positions of these markers are known in the digital model of the phantom. For each implanted k-wire, four distances were measured from a reference point located at the proximal end of the wire. Manual measurements were obtained using digital vernier calipers. The same set of distances was also automatically recorded by the simulation system. Figure 16 illustrates the distance measurement acquisition using both the system and the digital vernier caliper. These measurements are crucial as they reflect the matching characteristics between the digital and physical models. Each measurement method has inherent limitations. Manual caliper measurements are susceptible to human reading error but can detect deviations in phantom reproduction, including within the soft tissue. The simulation system, however, relies on marker-based tracking rigidly coupled to the phantom's hard components. Specifically, the implanted k-wire's alignment with the phantom's internal hard components provides insight into how well the digital model aligns with the physical phantom, even for non-visible components. This alignment assessment is crucial for understanding the relationship between the digital surgical plan and the actual k-wire position, especially for anatomical structures obscured during the procedure.

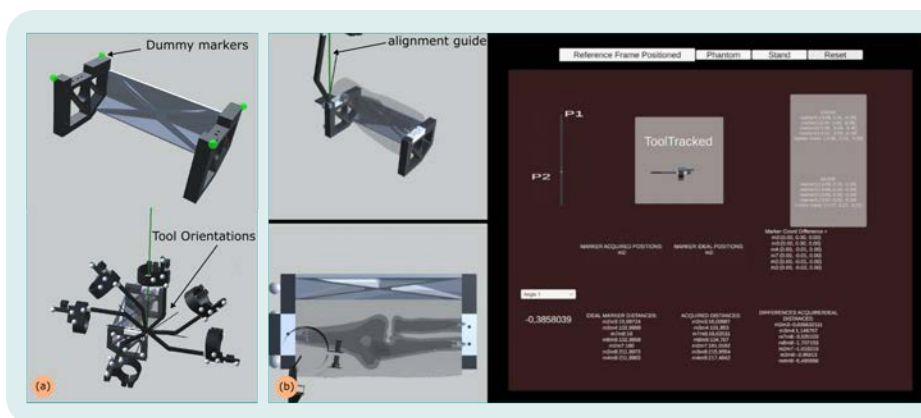


**Fig. 17:** In figure: (a) fiducial points and tool poses for performance evaluation; (b) accuracy tool interface

ASTM F2554-10 standardizes how to assess the positional accuracy of computer-assisted surgical systems. Based on the indication prescribed by the Standard in the framework is indicated the evaluation of the *location of a point relative to a coordinate system*, *relative point to point accuracy (linear)*, and *repeatability of coordinates of a single point* and for optically based system, the range of visible orientations of the reference frame or tools [57]. To overcome the lacking of the phantom proposed by the Standard the *system's static performance*, including accuracy and precision, was quantified through 3D-printed fiducial markers mapped to spatial coordinates. To evaluate

the dependence of the tracking tool orientation (angular position) on performance it is manipulated along a point, associated with a dummy marker. To evaluate the distance dependence of camera to phantom in the working volume, acquisition was repeated in the range 0.3m-0.6m. Distance was determined by averaging z-coordinates of stand markers. Integration of Standard’s principle are guided thorough a Unity-based interface. This guide the tracking tool positioning, automate data collection and recording (Figure 17).

### 3 Results

The described system represent a Computer Integrated System (CIS). The multiplatform integration make crucial the evaluation of the errors and accuracies at different levels [58]. Haidegger et al. [59] distinguish three different types of accuracies in terms of spatial errors. Accuracy and repeatability define the precision of CIS. This precision is influenced by encoder resolution, hardware compliance (e.g., servos), and structural rigidity. *Intrinsic accuracy* (0.1–0.6 mm) is the average operational error of a component (eg. random errors, imaging device resolution, noise etc.). *Registration errors* (0.2–3 mm) arise from residual errors in computational methods. *Application accuracy* (0.6–10 mm) measures the integrated system’s overall targeting error in clinical procedures or mock setups. This metric validates the system’s task-specific effectiveness.

#### 3.1 Intrinsic Accuracy

Systematic error was measured at 500mm and 1000mm, distances determined relative to a point of interest within a defined frame area. A laser meter (2mm accuracy) provided ground truth measurements. Systematic error is affected by distance, changing by 1.763 mm, whereas random error remains relatively stable, changing by only 0.159 mm. In Figure 18 the distribution of these measurement errors is plotted in a plane aligned with the point of interest. It is evident how, in case of systematic error (left), for both 500 and 1000mm, the error increases linearly as a function of the distance from the point of interest (blue to red in the 3D plot). On the other hand, the random error (left) remains stable, without an evident visual pattern in the 3D plot.

distance Camera - POI	Systematic Error (mm)	Random Error (mm)
500 mm	0.486	0.522
1000 mm	-1.277	0.681

**Table 4:** Kinect Azure DK Random and Systematic Errors

#### 3.2 Application Accuracy

The *Point’s Relative Location in a Coordinate System* measures the system’s ability to determine the position of a specific point in 3D space, such as the tip of a K-wire or an anatomical landmark. This is crucial for ensuring correct k-Wire placement relative to the patient’s anatomy, reducing the risk of errors. It is assessed by analyzing

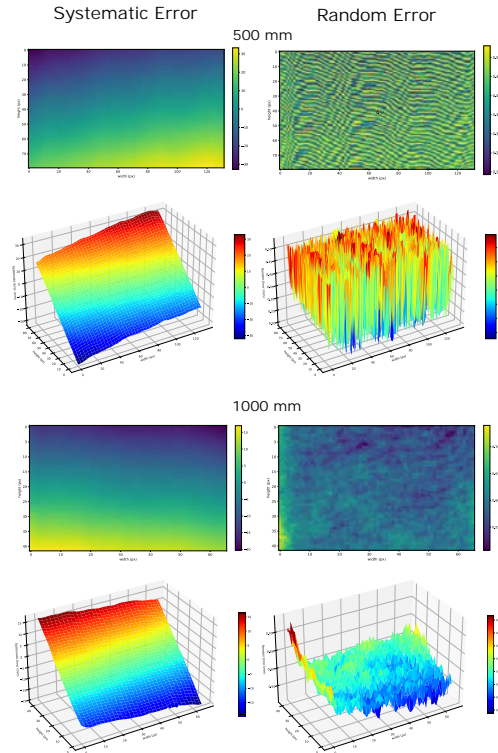


**Fig. 18:** Depth Camera Systematic and Random Errors.

the relative positions acquired in relation to fiducial markers. Each fiducial marker location is the origin of the reference system. The *mean acquisition error*, defined as the Euclidean distance between acquired point coordinates and the ideal fiducial marker location, demonstrated minimal fluctuation across varying camera distances (Figure 19a). Mean error values ranged from 5.29 mm at 0.6m to 6.15 mm at 0.4m, suggesting negligible distance-related impact on the tracking system’s accuracy. *Standard deviation*, indicative of the system’s consistency, varied from 2.13 mm (highest consistency) at 0.3m to 3.43 mm (most variability) at 0.5m, implying potential distance influence on tracking system consistency. Figure 19b illustrates the variability and precision of measurements across tracking tool poses. It shows that tool positioning not influences substantially the measurement precision. Table 5 presents the mean deviations along the x, y, and z axes for varying camera distances (0.3m-0.6m).

For each axis, the differences in error across camera distances were not statistically significant. Notably, the mean deviation was largest along the x-axis (approximately 3 mm) and smallest along the z-axis.

The *Repeatability of Single-Point Coordinates* assesses the system’s ability to consistently detect the position of a specific point in repeated measurements. This ensures

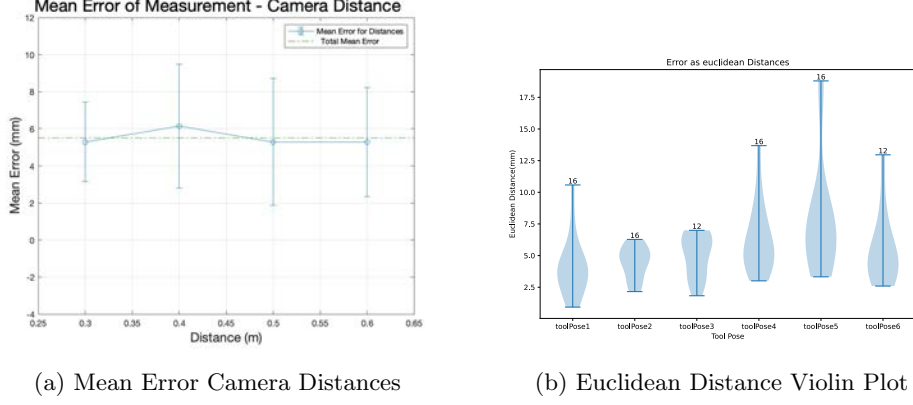


**Fig. 19:** Euclidean distance error - Tool Pose

Cam Dist (m)	$\Delta x_{\text{Mean}} \pm \text{SE}(\text{mm})$	$\Delta y_{\text{Mean}} \pm \text{SE}(\text{mm})$	$\Delta z_{\text{Mean}} \pm \text{SE}(\text{mm})$
0.3	$3.199 \pm 0.438$	$2.550 \pm 0.537$	$2.149 \pm 0.499$
0.4	$3.754 \pm 0.397$	$2.628 \pm 0.420$	$2.920 \pm 0.701$
0.5	$3.732 \pm 0.000$	$2.452 \pm 0.000$	$1.679 \pm 0.000$
0.6	$3.284 \pm 0.575$	$2.594 \pm 0.504$	$1.962 \pm 0.250$

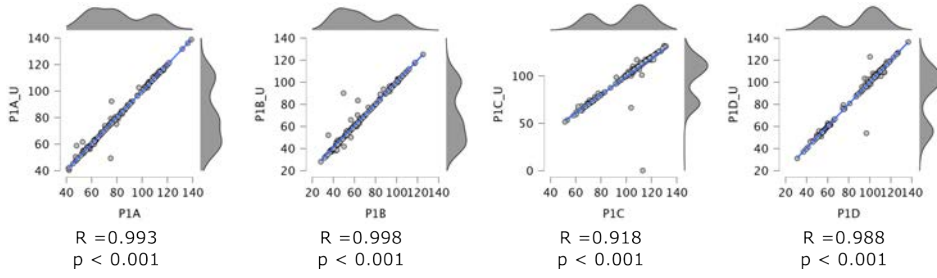
**Table 5:** Coordinates error in x,y,z at different camera distances: 0.3m (N=16); 0.4m (N=24); 0.5m (N=24); 0.6m (N=24)

the stability and reliability of the AR’s visual information during surgery, allowing the surgeon to perform the procedure with greater precision. It is examined at each acquisition distance, with system recalibration via fiducial marker coordinate updates after distance changes. Table 6 reports the standard deviation of deviations for each coordinate. Results highlight higher repeatability along the z-axis compared to the x and y axes.

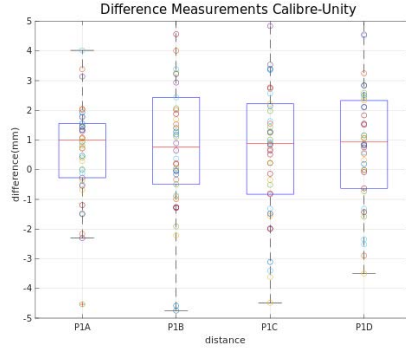
**Table 6:** Standard deviation of measurements at different distances (mm): 0.3m (N=16); 0.4m (N=24); 0.5m (N=24); 0.6m (N=24)

Dist.	P1			P2			P3			P4		
	x	y	z	x	y	z	x	y	z	x	y	z
30cm	5.048	4.023	3.113	5.033	1.017	1.079	1.853	1.090	0.377	1.059	0.575	1.364
40cm	3.565	3.823	2.975	3.065	1.211	1.809	0.682	2.479	1.726	1.434	3.341	6.107
50cm	2.843	2.485	0.693	2.526	3.062	1.631	2.760	2.411	1.475	6.254	2.810	2.091
60cm	1.499	3.320	1.409	1.621	2.034	1.031	1.298	4.608	1.346	3.828	4.661	2.832

The *Relative Point-to-Point Accuracy* measures the AR system’s ability to accurately determine the distance between two points in space. This is crucial for assessing



(a) Correlation Plot between navigation system measurements and caliper acquired ones (N = 198)



(b) N=14 for each distance

**Fig. 20:** Comparison between caliper and Automatic Distance Acquisition.

Difference	P1A	P1B	P1C	P1D	All
<b>Mean(mm)</b>	0.9381	1.4030	0.8783	0.8709	1.0226
<b>SD(mm)</b>	2.3243	3.6618	2.7053	2.4700	2.8217

**Table 7:** Mean and Standard Deviation Difference Values (N=42 for each distance)

the precision of K-wire insertion and its relationship to surrounding anatomical structures. It was evaluated by comparing measured distances to known distances for both fiducial point-derived distances and caliper/automated system measurements on the inserted k-wire. The simulation phantom, containing ten circumferential markers, was used for the insertion of 45 k-wires. For each k-Wire, four distances were measured from the posterior extremity to four selected markers using both a manual gauge and the developed automated system. Figure 20 and Table 7 present a comparison of measurement discrepancies across four distances using manual and automatic methods. The box plots in Figure 20a shows a symmetrical distribution of measurement differences around the zero line, with varying degrees of spread indicated by the range and outliers. Overall, the mean discrepancy is slightly over 1 mm with a variability of about

2.8 mm. Increasing the distance between measured points negatively impacts relative point-to-point accuracy, while increasing the acquisition setup distance improves accuracy. This is attributed to the use of wide field-of-view mode, where optical distortion is more pronounced at shorter distances. Comparison of automatic and manual measurements reveals mean differences ranging from 0.87 mm to 1.40 mm, and standard deviations from 2.32 mm to 3.66 mm. The overall mean difference is 1.02 mm with a standard deviation of 2.82 mm. Notably, the standard deviation across targets between the two methods is nearly identical, indicating the automatic system’s ability for consistent measurement reproduction. The comparison also shows similar deviations, with offsets at individual points minimally affecting distance calculations.

### 3.3 Qualitative assesment of system usability

To assess the subjective performance of the system, we conducted a qualitative evaluation of the setup. N=14 expert orthopedic surgeons ( $\geq 5$  years of experience) were challenged to place a k-wire from the medial to the lateral epicondyle of the humerus. Both the target position and the surgical drill were tracked using our setup, as illustrated in figure 2. Experts then evaluated the three key features of the setup: the X-ray simulation system, the augmented reality (AR) system and the phantom model. The participants were then asked to answer to a SUS (system usability scale) questionnaire (Table 8).

SUS Question	Rating (0 to 5)	SE
How realistic is the X-Ray Simulation?	4.07	0.78
X-Ray Simulator Quality	[HTML]FFFFFF3.92	0.91
How comfortable is the use of the X-Ray simulator?	4.21	0.89
How realistic the AR simulator feels like?	4	0.74
Which is the overall quality of the AR simulation?	[HTML]FFFFFF4.14	1.01
How comfortable is the use of the AR Goggles?	[HTML]FFFFFF3.78	1.02
How realistic if the physical phantom?	3.78	0.89
[HTML]FFFFFFWhich is the overall quality of the physical phantom?	[HTML]FFFFFF4.21	0.89

**Table 8:** SUS Questionnaire

For each component, three parameters were evaluated: realism, simulation quality, and comfort. *Realism*: participants rated how closely each system resembled its real-world counterpart, on a scale from 0 (completely unrealistic) to 5 (indistinguishable from reality). *Simulation Quality*: this parameter evaluated the utility of the system for training purposes, rated from 0 (completely dissimilar to real procedures) to 5 (indistinguishable from actual procedures). *Comfort*: participants rated their ease of interaction with the system, where 0 indicated extreme discomfort (e.g., unusable for more than a minute) and 5 indicated high comfort (e.g., usable for extended periods). Comfort ratings for the phantom model were not applicable and thus excluded. Results for each parameter were averaged across participants (Table 8).

## 4 Discussion

Efficient workflow and patient safety are fundamental principles in traditional operating room design [60]. The arrangement of operating room components is essential for maintaining sterility, ensuring efficient communication, and providing immediate access to necessary tools during surgery [61, 62]. In simulated environment, a surgical field comprising only the essential elements is practical and effective [25]. In line with Aumann this reduction maintains the core functionalities essential for the procedure allowing for focused assessment of AR in surgical training, avoiding the complexities and costs of a full-scale operating room [63]. This approach ensures effective training while maintaining a controlled and repeatable simulation environment [26, 27].

Object pose estimation, the determination of an object’s position and orientation in 3D space, can be achieved through various methods. These methods rely on mechanical, acoustic, inertial, magnetic, or radio frequency principles [64, 65]. Among these, optical tracking systems (OTS) are prevalent in fields like computer-assisted surgery, neurosurgery, industrial applications, and virtual reality [66]. OTSs fundamentally consist of signal sources, sensors, and a data acquisition/processing system. They operate in two main configurations: inside-looking-out and outside-looking-in. Inside-looking-out systems track a camera’s movement relative to fixed references, while outside-looking-in systems utilize external cameras to track a marked target. The latter is generally favored for tracking multiple objects, each uniquely identified by an optical pattern. Commercially available OTSs include the Polaris and Optotrak series (Northern Digital Inc.) for motion capture and biomechanical analysis, the MicronTracker series (ClaroNav) for clinical use, and the FusionTrack systems (Atracsys) [66]. However, these systems typically exhibit tracking errors in the millimeter to centimeter range [30, 67–69]. Furthermore, they have limited tracking capacity and high costs due to the complexity of pose estimation calculations, which rely on triangulation using marker geometry, activation sequence, and sensor distances [66]. For mobile AR experiences, marker-based inside-out tracking is commonly employed, facilitated by libraries like ARToolKit, ArUco, and PTC Vuforia. These systems estimate object pose by attaching fiducial markers to it [19]. However, a previously described tracking method [70] proved unsuitable for our framework due to occlusion problems and incompatibility with surgical workflows.

System development and evaluation revealed that the augmented reality platform’s hardware requirements are incompatible with the goal of integrating the framework into a single device. The current two-phase system, reliant on a reference frame and navigation tool tracking, is prone to user error. Additionally, the use of spheres for recognition and visualization may be suboptimal. System complexity increases cognitive load during pre-testing, necessitating simplified interactions and an improved user interface with intuitive gestures to facilitate learning and use.

Figure 21 illustrates how error generation is a multifactorial process. Starting from the CAD model, the tracking tool is generated for manufacturing. The markers, being variably assembled and subject to greater wear than other rigid components,

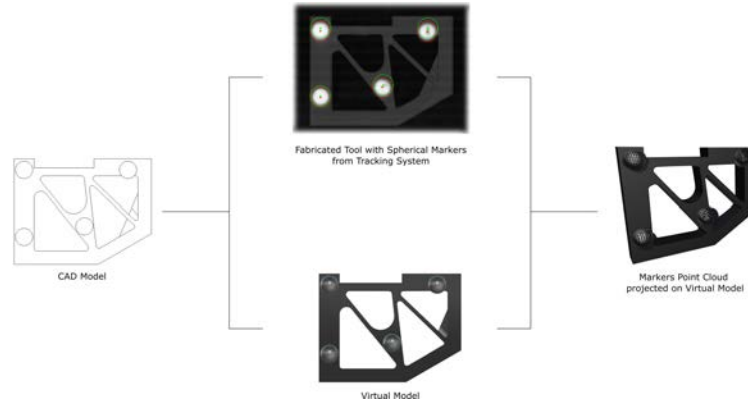


**Fig. 21:** Tracking Errors Components Errors

and significantly affecting the coherence between real and digital data, constitute the primary source of error generation and propagation. Added to this is the image generation and its conversion into a depth map. It is therefore crucial to study how the data texture varies according to environmental conditions and camera settings. Depth data must be converted into a point cloud using a calibration matrix. The calibration parameters vary depending on environmental conditions. For greater accuracy, the system should be recalibrated with each use, but this would compromise the usability of the platform. A further error is the generation and 3D transformation into point clusters. The algorithm for calculating centroids represents an additional component of analysis. Finally, the use of dynamic filters, such as the Kalman filter, introduces variability in the acquired data, altering the correspondence with reality, although it improves visual perception.

Integration of neural networks for image processing is expected to improve system accuracy and adaptability through new computer vision techniques and modeling methods. Using neural networks in the tracking and visualization system can improve its performance. Studying AI-based marker and markerless tracking techniques is crucial. Marker occlusion is a common issue with current viewers. These techniques reduce both computational cost (important for integrating visualization, tracking, and computation onto a single platform) and the occlusion problem, expanding the system's field of view. Feed-forward integration enhances the user experience. Furthermore, neural networks allow rendering of 2D objects from 3D models, benefiting from real-time data for greater coherence between reality and digital information.

The system described was developed to simulate a specific scenario of a K-wire percutaneous implant. Overall, the systems showed consistent performance, with a good level of appreciation from expert users, evaluated qualitatively using an SUS questionnaire (Table 8). Average scores for realism, simulation quality, and comfort were generally positive, averaging approximately 80% of the maximum possible score. This indicates good, though not optimal, levels of realism and simulation quality. In

particular, the results highlighted that:

- X-ray simulation comfort achieved the highest average score (green, 4.21, 84.3%);
- AR simulation quality showed the strongest performance among AR parameters (4.14, 82.9%);
- Phantom realism and simulation quality were lower than those of the X-ray and AR systems, with realism averaging 3.78 (red, 75.7%).

These findings suggest that while the systems are effective for training purposes, further refinements could enhance their realism and user experience.

Although the described system accurately simulates the variable of augmented reality and the X-ray use in the operating room (OR), it eliminates several variables associated with the real environment. Each block presented in Table 1 introduces a question with an answer including a caveat, compared to the real world. For example, it is necessary to answer questions such as "What are the main steps to perform during the simulation?" or "Which model should be used to simulate the patient scenario?". In these terms, the environmental stressors of the OR that might impact the performance and the outcome of the surgery, are not present in an artifact situation. Also, no matter how realistic the anatomical dummy is, one expert surgeon would still perceive subtle differences with a real patient, both because of its physical characteristics, and because, psychologically, a real patient is not present. Some, however, could be implemented in future developments. The introduction of spatial sounds that reduce attention to the procedure being performed or visual stimuli in the wide range of vision can be implemented to overcome some of the limitations of the current version.

The current interface presents limitations in user interaction. Users unfamiliar with augmented reality platforms may find interacting with spatial elements challenging. This is particularly true for buttons and scrolling menus. Potential improvements include: Integrating voice commands to supplement or replace physical interaction; Enabling on-site scene customization to address limitations in element display due to environmental factors that reduce holographic display effectiveness; For critical components, incorporating interaction elements with materials and object shaders within the scene.

The presented system is in line with the main works that are on the same line of development and presented in the Table 2. According to the acquired experimental data, there is an application accuracy, i.e., associated with use, of 1.02 mm. Accuracy should be studied at various levels to limit sources of error as much as possible. That date, however, represents the end point of error propagation, so it is well representative of system performance.

## 5 Conclusion

Here, we developed, and described in detail, a cost-effective system to simulate minimally invasive orthopedic surgery. The use of the Kinect Azure DK as an IR camera enabled the development of a system based on spherical markers. Augmented reality integration was achieved using HoloLens 2. The use of an external PC as the processing unit allowed for the creation of a fluid and user-friendly virtual simulation environment. This system allows surgeon trainees and students to gain hands-on practice. Thanks to the affordability of the system, we can envision a diffused use of this technology for larger classrooms, and for non experts as well. Widespread use of this technology can improve the overall surgical skills. Integrating these emerging technologies into training will enhance healthcare performance, making procedures safer and more cost-effective. Extensive testing with surgical trainees will be conducted as our next research phase to validate the system's effectiveness in clinical training.

## 6 Conflict of interest statement

CC declares that he is a co-founder of the university spinoff "Intravides"

## 7 Acknowledgments

This work was funded by NODES project funded by the MUR – M4C2 1.5 of PNRR with grant agreement n. ECS00000036 and the Grant for Internationalization Fund of the University of Turin to CC.

## References

- [1] Treuting, R.: Minimally invasive orthopedic surgery: Arthroscopy. *The Ochsner Journal* **2**(3), 158
- [2] Dalmau-Pastor, M., Vega, J., Malagelada, F., Peña, F., Manzanares-Céspedes, M.C.: An anatomical study of nerves at risk during minimally invasive hallux valgus surgery. *Journal of Visualized Experiments* (132) (2018) <https://doi.org/10.3791/56232>
- [3] Cangelosi, A., Riberi, G., Salvi, M., Molinari, F., Titolo, P., Agus, M., Cali, C.: Mixed Reality for Orthopedic Elbow Surgery Training and Operating Room Applications: A Preliminary Analysis. In: Banterle, F., Caggianese, G., Capece, N., Erra, U., Lupinetti, K., Manfredi, G. (eds.) *Smart Tools and Applications in Graphics - Eurographics Italian Chapter Conference*. The Eurographics Association, ??? (2023). <https://doi.org/10.2312/stag.20231291>
- [4] Sharma, H., Taylor, G., Clarke, N.: A review of k-wire related complications in the emergency management of paediatric upper extremity trauma. *The Annals of The Royal College of Surgeons of England* **89**(3), 252–258 (2007) <https://doi.org/10.1308/003588407x155482>

- [5] Zang, J., Lin, Z., Ding, C., Bian, D., Pan, J., Tang, X.: Augmented reality navigation for precise implantation of l2 pelvic tunnel screws in minimally invasive surgery. *Fundamental Research* (2024) <https://doi.org/10.1016/j.fmre.2024.05.010>
- [6] Charles, A.J., Luo, E., Arango, A., Rowe, D., Goodwin, C.R., Erickson, M.M.: Augmented reality in spine surgery narrative review: Seeing is believing. *Operative Techniques in Orthopaedics* **33**(4), 101068 (2023) <https://doi.org/10.1016/j.oto.2023.101068>
- [7] Cofano, F., Di Perna, G., Bozzaro, M., Longo, A., Marengo, N., Zenga, F., Zullo, N., Cavalieri, M., Damiani, L., Boges, D.J., *et al.*: Augmented reality in medical practice: from spine surgery to remote assistance. *Frontiers in Surgery* **8**, 657901 (2021)
- [8] Birlo, M., Edwards, P.J.E., Clarkson, M., Stoyanov, D.: Utility of optical see-through head mounted displays in augmented reality-assisted surgery: A systematic review. *Medical Image Analysis* **77**, 102361 (2022) <https://doi.org/10.1016/j.media.2022.102361>
- [9] Fida, B., Cutolo, F., Franco, G., Ferrari, M., Ferrari, V.: Augmented reality in open surgery. *Updates in Surgery* **70**(3), 389–400 (2018) <https://doi.org/10.1007/s13304-018-0567-8>
- [10] De Paolis, L.T., Aloisio, G.: Augmented Reality in Minimally Invasive Surgery, pp. 305–320. Springer, ??? (2010). [https://doi.org/10.1007/978-3-642-05167-8\\_17](https://doi.org/10.1007/978-3-642-05167-8_17). [http://dx.doi.org/10.1007/978-3-642-05167-8\\_17](http://dx.doi.org/10.1007/978-3-642-05167-8_17)
- [11] PETERS, T.M.: Image-guided surgery: From x-rays to virtual reality. *Computer Methods in Biomechanics and Biomedical Engineering* **4**(1), 27–57 (2001) <https://doi.org/10.1080/10255840008907997>
- [12] Rowantree, S.A., Currie, C.: Orthopaedic surgeons’ knowledge and practice of radiation safety when using fluoroscopy during procedures: A narrative review. *Radiography* **30**(1), 274–281 (2024) <https://doi.org/10.1016/j.radi.2023.11.017>
- [13] Kalteis, T., Handel, M., B athis, H., Perlick, L., Tingart, M., Grifka, J.: Imageless navigation for insertion of the acetabular component in total hip arthroplasty: is it as accurate as ct-based navigation? *The Journal of Bone & Joint Surgery British Volume* **88**(2), 163–167 (2006)
- [14] Richter, M., Zech, S.: 3d imaging (arcadis)-based computer assisted surgery (cas) guided retrograde drilling in osteochondritis dissecans of the talus. *Foot & ankle international* **29**(12), 1243–1248 (2008)
- [15] Gonschorek, O., Hauck, S., Spiegl, U., Wei , T., P atzold, R., B uhren, V.: O-arm -based spinal navigation and intraoperative 3d-imaging: first experiences.

- [16] Kelft, E., Costa, F., Planken, D., Schils, F.: A prospective multicenter registry on the accuracy of pedicle screw placement in the thoracic, lumbar, and sacral levels with the use of the o-arm imaging system and stealthstation navigation. *Spine* **37**(25), 1580–1587 (2012)
- [17] Carelsen, B., Haverlag, R., Ubbink, D.T., Luitse, J.S., Goslings, J.C.: Does intra-operative fluoroscopic 3d imaging provide extra information for fracture surgery? *Archives of orthopaedic and trauma surgery* **128**, 1419–1424 (2008)
- [18] Zwingmann, J., Konrad, G., Mehlhorn, A., Südkamp, N., Oberst, M.: Percutaneous iliosacral screw insertion: malpositioning and revision rate of screws with regards to application technique (navigated vs. conventional). *Journal of Trauma and Acute Care Surgery* **69**(6), 1501–1506 (2010)
- [19] Yaniv, Z.: Registration for orthopaedic interventions. *Lecture Notes in Computational Vision and Biomechanics* **23**, 41–70 (2016) [https://doi.org/10.1007/978-3-319-23482-3\\_3](https://doi.org/10.1007/978-3-319-23482-3_3)
- [20] Barcali, E., Iadanza, E., Manetti, L., Francia, P., Nardi, C., Bocchi, L.: Augmented reality in surgery: A scoping review. *Applied Sciences* **12**(14), 6890 (2022) <https://doi.org/10.3390/app12146890>
- [21] Shuhaiber, J.H.: Augmented reality in surgery. *Archives of Surgery* **139**(2), 170 (2004) <https://doi.org/10.1001/archsurg.139.2.170>
- [22] Kanno, H., Handa, K., Murotani, M., Ozawa, H.: A novel intraoperative ct navigation system for spinal fusion surgery in lumbar degenerative disease: Accuracy and safety of pedicle screw placement. *Journal of Clinical Medicine* **13**(7), 2105 (2024) <https://doi.org/10.3390/jcm13072105>
- [23] Rojas, J.T., Läderrmann, A., Ho, S.W.L., Rashid, M.S., Zumstein, M.A.: Glenoid component placement assisted by augmented reality through a head-mounted display during reverse shoulder arthroplasty. *Arthroscopy Techniques* **11**(5), 863–874 (2022) <https://doi.org/10.1016/j.eats.2021.12.046>
- [24] Dominique, G., Kunitsky, K., Natchagande, G., Jalloh, M., Gebreamlak, A.L., Lawal, I., Agoukpe, M.M., Hodonou, F.D., Yevi, D.M.I., Avakoudjo, J.D.G., McCammon, K., Watson, G., Scotland, K.B.: Evaluation of augmented reality technology in global urologic surgery. *The American Journal of Surgery* **226**(4), 471–476 (2023) <https://doi.org/10.1016/j.amjsurg.2023.05.014>
- [25] Cardoso, S.A., Suyambu, J., Iqbal, J., Cortes Jaimes, D.C., Amin, A., Sikto, J.T., Valderrama, M., Aulakh, S.S., Ramana, V., Shaukat, B., Patel, T.: Exploring the role of simulation training in improving surgical skills among residents: A narrative review. *Cureus* (2023) <https://doi.org/10.7759/cureus.44654>

- [26] Ziv: Patient safety and simulation-based medical education. *Medical Teacher* **22**(5), 489–495 (2000) <https://doi.org/10.1080/01421590050110777>
- [27] Tan, S.S.Y., Sarker, S.K.: Simulation in surgery: a review. *Scottish Medical Journal* **56**(2), 104–109 (2011) <https://doi.org/10.1258/smj.2011.011098>
- [28] Lembo, D., Abate Daga, F., Calì, C., Garbossa, D., Manfredi, M., Odetto, L., Ostacoli, L., Paccotti, P., Raimondo, S., Reimondo, G., Sciascia, S.: Early introduction of simulation in the medical curriculum: the medinto perspective. *Frontiers in Medicine* **10** (2024) <https://doi.org/10.3389/fmed.2023.1280592>
- [29] Cutolo, F.: Letter to the editor on “augmented reality based navigation for computer assisted hip resurfacing: A proof of concept study”. *Annals of Biomedical Engineering* **47**(11), 2151–2153 (2019) <https://doi.org/10.1007/s10439-019-02299-w>
- [30] Gsaxner, C., Li, J., Pepe, A., Schmalstieg, D., Egger, J.: Inside-out instrument tracking for surgical navigation in augmented reality. In: Proceedings of the 27th ACM Symposium on Virtual Reality Software and Technology. VRST '21. ACM, ??? (2021). <https://doi.org/10.1145/3489849.3489863> . <http://dx.doi.org/10.1145/3489849.3489863>
- [31] Hajek, J., Unberath, M., Fotouhi, J., Bier, B., Lee, S.C., Osgood, G., Maier, A., Armand, M., Navab, N.: Closing the Calibration Loop: An Inside-Out-Tracking Paradigm for Augmented Reality in Orthopedic Surgery, pp. 299–306. Springer, ??? (2018). [https://doi.org/10.1007/978-3-030-00937-3\\_35](https://doi.org/10.1007/978-3-030-00937-3_35) . [http://dx.doi.org/10.1007/978-3-030-00937-3\\_35](http://dx.doi.org/10.1007/978-3-030-00937-3_35)
- [32] Wang, L., Sun, Z., Zhang, X., Sun, Z., Wang, J.: A HoloLens Based Augmented Reality Navigation System for Minimally Invasive Total Knee Arthroplasty, pp. 519–530. Springer, ??? (2019). [https://doi.org/10.1007/978-3-030-27529-7\\_44](https://doi.org/10.1007/978-3-030-27529-7_44) . [http://dx.doi.org/10.1007/978-3-030-27529-7\\_44](http://dx.doi.org/10.1007/978-3-030-27529-7_44)
- [33] Cutolo, F., Fida, B., Cattari, N., Ferrari, V.: Software framework for customized augmented reality headsets in medicine. *IEEE Access* **8**, 706–720 (2020) <https://doi.org/10.1109/ACCESS.2019.2962122>
- [34] Hu, X., Baena, F.R.y., Cutolo, F.: Head-mounted augmented reality platform for markerless orthopaedic navigation. *IEEE Journal of Biomedical and Health Informatics* **26**(2), 910–921 (2022) <https://doi.org/10.1109/JBHI.2021.3088442>
- [35] Ma, L., Huang, T., Wang, J., Liao, H.: Visualization, registration and tracking techniques for augmented reality guided surgery: a review. *Physics in Medicine and Biology* **68**(4), 04–02 (2022) <https://doi.org/10.1088/1361-6560/acaf23>
- [36] Ulrich, L., Salerno, F., Moos, S., Vezzetti, E.: How to exploit augmented reality (ar) technology in patient customized surgical tools: a focus on

osteotomies. *Multimedia Tools and Applications* (2024) <https://doi.org/10.1007/s11042-023-18058-y>

- [37] Chen, X., Xu, L., Wang, Y., Wang, H., Wang, F., Zeng, X., Wang, Q., Egger, J.: Development of a surgical navigation system based on augmented reality using an optical see-through head-mounted display. *Journal of biomedical informatics* **55**, 124–131 (2015)
- [38] Gsaxner, C., Li, J., Pepe, A., Schmalstieg, D., Egger, J.: Inside-out instrument tracking for surgical navigation in augmented reality. In: *Proceedings of the 27th ACM Symposium on Virtual Reality Software and Technology*, pp. 1–11 (2021)
- [39] Zang, J., Lin, Z., Ding, C., Bian, D., Pan, J., Tang, X.: Augmented reality navigation for precise implantation of l2 pelvic tunnel screws in minimally invasive surgery. *Fundamental Research* (2024)
- [40] Martin-Gomez, A., Li, H., Song, T., Yang, S., Wang, G., Ding, H., Navab, N., Zhao, Z., Armand, M.: STTAR: surgical tool tracking using off-the-shelf augmented reality head-mounted displays. *IEEE* (2023)
- [41] Yang, R., Wang, Z., Liu, S., Wu, X.: Design of an accurate near infrared optical tracking system in surgical navigation. *Journal of Lightwave Technology* **31**(2), 223–231 (2013) <https://doi.org/10.1109/JLT.2012.2227943>
- [42] Microsoft: Microsoft’s Azure Kinect Developer Kit Technology Transfers to Partner Ecosystem. Tech Community. <https://techcommunity.microsoft.com/blog/themixedrealityblog/microsoft%E2%80%99s-azure-kinect-developer-kit-technology-transfers-to-partner-ecosystem/3899122>
- [43] qm13: Azure Kinect DK documentation — Microsoft Learn. <https://learn.microsoft.com/en-us/azure/kinect-dk/>. Accessed: 2024-07-03 (2024)
- [44] Depth Camera D435i – Intel® RealSense™ Depth and Tracking Cameras. <https://www.intelrealsense.com/depth-camera-d435i/>. Accessed: 2024-07-03 (2024)
- [45] Rijal, S., Pokhrel, S., Om, M., Ojha, V.: Comparing depth estimation of azure kinect and realsense d435i cameras. In: *International Congress on Information and Communication Technology*, pp. 225–235 (2024). Springer
- [46] Bamji, C.S., Mehta, S., Thompson, B., Elkhatib, T., Wurster, S., Akkaya, O., Payne, A., Godbaz, J., Fenton, M., Rajasekaran, V., Prather, L., Nagaraja, S., Mogallapu, V., Snow, D., McCauley, R., Mukadam, M., Agi, I., McCarthy, S., Xu, Z., Perry, T., Qian, W., Chan, V.-H., Adep, P., Ali, G., Ahmed, M., Mukherjee, A., Nayak, S., Gampell, D., Acharya, S., Kordus, L., O’Connor, P.: Impixel 65nm bsi 320mhz demodulated tof image sensor with 3m global shutter pixels and analog binning. In: *2018 IEEE International Solid-State Circuits Conference -*

- (ISSCC), pp. 94–96 (2018). <https://doi.org/10.1109/ISSCC.2018.8310200>
- [47] qm13: Azure Kinect DK documentation — Microsoft Learn. <https://learn.microsoft.com/en-us/previous-versions/azure/kinect-dk/>. Accessed: 2025-01-30 (2025)
- [48] CopyWalker: Kinect DK — Microsoft Learn. [https://learn.microsoft.com/en-us/product-style-guide-msft-internal/a\\_z\\_names\\_terms/k/kinect-dk](https://learn.microsoft.com/en-us/product-style-guide-msft-internal/a_z_names_terms/k/kinect-dk). Accessed: 2025-01-09 (2025)
- [49] Azure Kinect - DepthEngine. <https://github.com/microsoft/Azure-Kinect-Sensor-SDK/blob/develop/docs/depthengine.md>. Accessed: 2025-01-30 (2025)
- [50] Bevk, M., Kononenko, I.: A statistical approach to texture description of medical images: a preliminary study. In: Proceedings of 15th IEEE Symposium on Computer-Based Medical Systems (CBMS 2002), pp. 239–244 (2002). IEEE
- [51] tesych: Azure Kinect DK coordinate systems — Microsoft Learn. <https://learn.microsoft.com/en-us/previous-versions/azure/kinect-dk/coordinate-systems>. Accessed: 2025-01-23 (2025)
- [52] Technologies, U.: Unity - Manual: Rotation and orientation in Unity. <https://docs.unity3d.com/Manual/QuaternionAndEulerRotationsInUnity.html>. Accessed: 2025-01-23 (2025)
- [53] Taylor, R.H.: Medical robotics and computer-integrated interventional medicine **18**(2), 87–117 (2016) <https://doi.org/10.5759/JSCAS.18.87>
- [54] Schnetzke, M., Fuchs, J., Vetter, S.Y., Beisemann, N., Keil, H., Grützner, P.-A., Franke, J.: Intraoperative 3d imaging in the treatment of elbow fractures-a retrospective analysis of indications, intraoperative revision rates, and implications in 36 cases. *BMC Medical Imaging* **16**, 1–8 (2016)
- [55] Kervyn, G.: The first open source 3d atlas of human anatomy. *Acta Scientific Anatomy* **1**, 13–15 (2022)
- [56] lolambean: MRTK2-Unity Developer Documentation - MRTK 2 — Microsoft Learn. <https://learn.microsoft.com/en-us/windows/mixed-reality/mrtk-unity/mrtk2/?view=mrtkunity-2022-05>. Accessed: 2024-06-30 (2024)
- [57] F2554 Standard Practice for Measurement of Positional Accuracy of Computer Assisted Surgical Systems. <https://www.astm.org/f2554-10.html>. Accessed: 2024-07-22 (2024)
- [58] Haidegger, T.: Probabilistic method to improve the accuracy of computer-integrated surgical systems. *Acta Polytechnica Hungarica* (2019)

- [59] Haidegger, T., Kazanzides, P., Rudas, I.J., Benyó, B., Benyó, Z.: The importance of accuracy measurement standards for computer-integrated interventional systems. (2010). <https://api.semanticscholar.org/CorpusID:155491683>
- [60] STAHL, J., SANDBERG, W., DAILY, B., WIKLUND, R., EGAN, M., GOLDMAN, J., ISAACSON, K., GAZELLE, S., RATTNER, D.: Reorganizing patient care and workflow in the operating room: a cost-effectiveness study. *Surgery* **139**(6), 717–728 (2006) <https://doi.org/10.1016/j.surg.2005.12.006>
- [61] Kanich, D.G., Byrd, J.R.: How to increase efficiency in the operating room. *Surgical Clinics of North America* **76**(1), 161–173 (1996) [https://doi.org/10.1016/s0039-6109\(05\)70429-1](https://doi.org/10.1016/s0039-6109(05)70429-1)
- [62] Hussain, A.K., Kakakhel, M.M., Ashraf, M.F., Shahab, M., Ahmad, F., Luqman, F., Ahmad, M., Mohammed Nour, A., Varrassi, G., Kinger, S.: Innovative approaches to safe surgery: A narrative synthesis of best practices. *Cureus* (2023) <https://doi.org/10.7759/cureus.49723>
- [63] Aumann, C.A.: A methodology for developing simulation models of complex systems. *Ecological Modelling* **202**(3–4), 385–396 (2007) <https://doi.org/10.1016/j.ecolmodel.2006.11.005>
- [64] Sabatini, A.M.: Estimating three-dimensional orientation of human body parts by inertial/magnetic sensing. *Sensors* **11**(2), 1489–1525 (2011) <https://doi.org/10.3390/s110201489>
- [65] Welch, G., Foxlin, E.: Motion tracking: No silver bullet, but a respectable arsenal. *IEEE Computer graphics and Applications* **22**(6), 24–38 (2002)
- [66] Sorriento, A., Porfido, M.B., Mazzoleni, S., Calvosa, G., Tenucci, M., Ciuti, G., Dario, P.: Optical and electromagnetic tracking systems for biomedical applications: A critical review on potentialities and limitations. *IEEE Reviews in Biomedical Engineering* **13**, 212–232 (2020) <https://doi.org/10.1109/rbme.2019.2939091>
- [67] Abawi, D.F., Bienwald, J., Dörner, R.: Accuracy in optical tracking with fiducial markers: an accuracy function for artoolkit. *Third IEEE and ACM International Symposium on Mixed and Augmented Reality*, 260–261 (2004)
- [68] Brand, M., Wulff, L.A., Hamdani, Y., Schüppstuhl, T.: Accuracy of marker tracking on an optical see-through head mounted display. In: Schüppstuhl, T., Tracht, K., Henrich, D. (eds.) *Annals of Scientific Society for Assembly, Handling and Industrial Robotics*, pp. 21–31. Springer, Berlin, Heidelberg (2020). [https://doi.org/10.1007/978-3-662-61755-7\\_3](https://doi.org/10.1007/978-3-662-61755-7_3)
- [69] Cao, A., Dhanaliwala, A., Shi, J., Gade, T., Park, B.: Image-based marker tracking and registration for intraoperative 3D image-guided interventions using

augmented reality (2019). <https://arxiv.org/abs/1908.03237>

- [70] Cangelosi, A., Riberi, G., Salvi, M., Molinari, F., Titolo, P., Agus, M., Calì, C.: Mixed Reality for Orthopedic Elbow Surgery Training and Operating Room Applications: A Preliminary Analysis. In: Banterle, F., Caggianese, G., Capece, N., Erra, U., Lupinetti, K., Manfredi, G. (eds.) Smart Tools and Applications in Graphics - Eurographics Italian Chapter Conference. The Eurographics Association, ??? (2023). <https://doi.org/10.2312/stag.20231291>